Cell Reports
Physical Science

CellPress
OPEN ACCESS

Article

Traps in the spotlight: How traps affect the charge carrier dynamics in $Cs_2AgBiBr_6$ perovskite

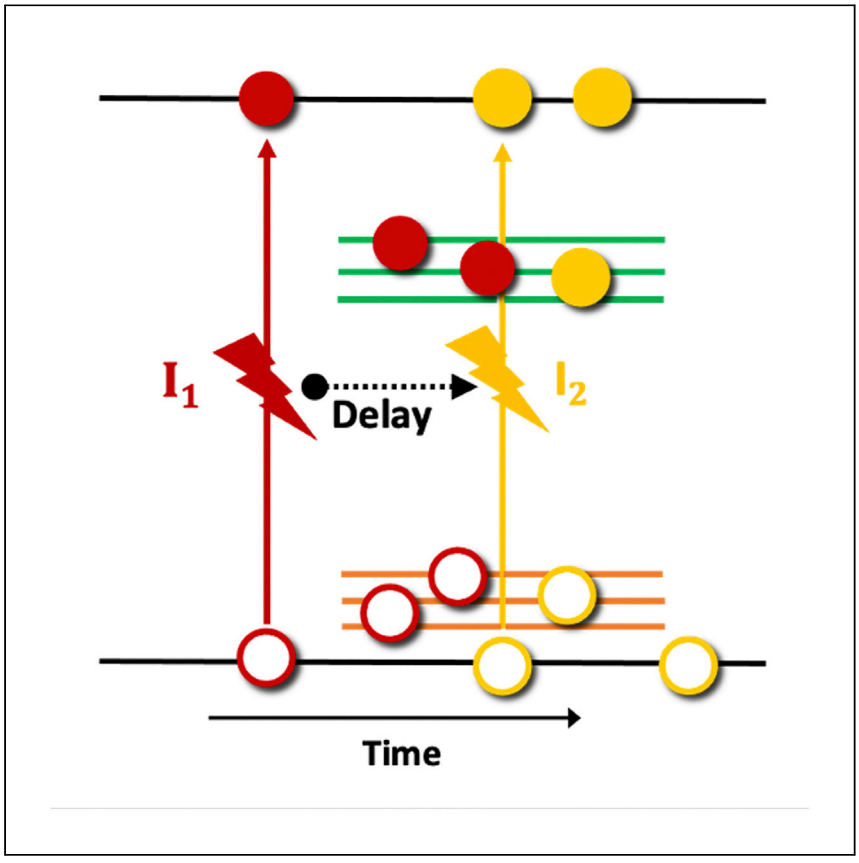

Trap-assisted electron recombination in $Cs_2AgBiBr_6$ thin films, combined with low hole mobility and shallow trapping, can be a major drawback of $Cs_2AgBiBr_6$ in photovoltaic devices. Caselli et al. reveal that the long-lived charge carriers in $Cs_2AgBiBr_6$ can offer a suitable, lead-free alternative for other applications, such as X-ray detectors or photocatalysis.

Valentina M. Caselli, Jos Thieme, Huygen J. Jöbsis, Sohan A. Phadke, Jiashang Zhao, Eline M. Hutter, Tom J. Savenije

t.j.savenije@tudelft.nl

Highlights

Double-pulse excitation TRMC is developed to study trapping processes

$Cs_2AgBiBr_6$ shows high photoconductance up to 30 μs after the first excitation

A high yield of free charges results from populated trap states by the first pulse

Emission of holes residing in shallow states extends over many microseconds

Caselli et al., Cell Reports Physical Science 3, 101055
October 19, 2022
https://doi.org/10.1016/j.xcrp.2022.101055

Cell Reports
Physical Science

CellPress
OPEN ACCESS

Article

Traps in the spotlight: How traps affect the charge carrier dynamics in $Cs_2AgBiBr_6$ perovskite

Valentina M. Caselli,[1] Jos Thieme,[1] Huygen J. Jöbsis,[2] Sohan A. Phadke,[1] Jiashang Zhao,[1] Eline M. Hutter,[2] and Tom J. Savenije[1,3,*]

SUMMARY

Suitable optoelectronic properties of lead halide perovskites make these materials interesting semiconductors for many applications. Toxic lead can be substituted by combining monovalent and trivalent cations, such as in $Cs_2AgBiBr_6$. However, efficiencies of $Cs_2AgBiBr_6$-based photovoltaics are still modest. To elucidate the loss mechanisms, in this report, we investigate charge dynamics in $Cs_2AgBiBr_6$ films by double-pulse excitation time-resolved microwave conductivity (DPE-TRMC). By exciting the sample with two laser pulses with identical wavelengths, we found a clear photoconductance enhancement induced by the second pulse even 30 μs after the first laser pulse. Modeling the DPE-TRMC results, complemented by photoluminescence and transient absorption, we reveal the presence of deep emissive electron traps, while shallow hole trapping is responsible for the long-lived transient absorption signals. These long-lived carriers offer interesting possibilities for X-ray detectors or photocatalysis. The DPE-TRMC methodology offers unique insight into the times involved in charge trapping and depopulation in $Cs_2AgBiBr_6$.

INTRODUCTION

Since their discovery as versatile semiconductors for photovoltaic applications, perovskite materials, with the general formula ABX_3, have been intensively studied. Tuning of their opto-electronic properties make it possible to reach remarkable power conversion efficiencies, currently topping out at 25.6%,[1] in roughly a decade of development. However, a rising concern regarding the use of lead in the photoactive layer has pushed research into lead-free alternative candidates. Attempts have been made to substitute the bivalent Pb^{2+} with alkaline metals[2,3] and homovalent Sn^{2+} or Ge^{2+}. Unfortunately, devices made with these elements show lower performances compared to their Pb analogs, and fast degradation.[4–7] Nonetheless, impressive efficiencies have been recently obtained with mixed Pb/Sn-based perovskites, despite the fast oxidation of the metal into Sn^{4+}.[8,9] Thanks to the flexibility of the perovskite structure also double-metal $A_2B'B''X_6$ perovskites can be synthesized. In these materials, the Pb^{2+} is replaced by a monovalent, B′, and a trivalent, B″, metal, present in the structure in an alternate fashion. Among them, $Cs_2AgBiBr_6$ is one of the most studied candidates, not only for photovoltaic applications but also for X-ray detection and photocatalysis.[10–15] This material can be synthetized via solution processes as well as by thermal evaporation.[13,16–18] At room temperature, it is present in its cubic phase, and shown to be thermodynamically more stable than lead-based perovskites.[13,17] However, power conversion efficiencies (PCEs) of devices based on double-metal perovskites are still below 3%.[13,17] The high and

[1]Department of Chemical Engineering, Delft University of Technology, van der Maasweg 9, 2629 HZ Delft, the Netherlands

[2]Inorganic Chemistry and Catalysis, Department of Chemistry, Utrecht University, Princetonlaan 8, 3584 CB Utrecht, the Netherlands

[3]Lead contact

*Correspondence: t.j.savenije@tudelft.nl

https://doi.org/10.1016/j.xcrp.2022.101055

indirect nature of its band gap, higher density of trap states, and lower charge carrier mobilities compared to Pb-based perovskite, have been argued as limiting factors of the performance in devices.[19]

Recent studies have shown that the strong electron-phonon coupling in $Cs_2AgBiBr_6$, even stronger than in the commonly applied and studied methylammonium lead iodide ($MAPbI_3$), could lead to self-trapping of the photoexcited charge carriers.[20] In $Cs_2AgBiBr_6$, self-trapping has been described as result of the formation of polarons, color centers, or even possibly self-trapped excitons.[20,21] Any of these processes could also be linked to the largely shifted and broad photoluminescence (PL) emission measured from $Cs_2AgBiBr_6$ samples.[20,21] Furthermore, a recent study by Wright et al. showed an ultrafast charge carrier trapping process (1 ps timescale) into localized states.[21] In contrast to such ultrafast dynamics in thin films, other reports have shown the presence of microsecond long-lived photoactive species by time-resolved photoluminescence (TRPL), transient absorption (TA), and time-resolved microwave conductivity (TRMC) measurements in powders and crystals.[16,22–24] To obtain a more complete model describing the photophysical processes in $Cs_2AgBiBr_6$, an in-depth study of the impact of these long-lived species on the charge carrier dynamics in $Cs_2AgBiBr_6$ is necessary.

This work aims to provide insights into the nature of these states and their influence on the charge carrier dynamics in $Cs_2AgBiBr_6$ thin films. To do so, we investigated $Cs_2AgBiBr_6$ thin films by means of TRPL, TA measurements, and double-pulse excitation-time-resolved microwave conductivity (DPE-TRMC), a new technique whose working principle is detailed in the experimental procedures. Basically, in DPE-TRMC the sample is illuminated by two laser pulses arriving with a short time delay. By comparing the photoconductance traces induced by the second pulse in the presence and absence of the first pulse, we are able to examine the effect of the long-lived species on the charge carrier dynamics. For these experiments, we used identical excitation wavelengths for both laser pulses but varying intensities and delay times. We modeled the results introducing a comprehensive model, which accounts for the free carrier generation yield, localization of free carriers, electron trapping by color centers, and shallow trap states for holes. The iterative analysis of the DPE-TRMC experiments with different intensities and delay times reveals the presence of a high concentration of both electron (10^{15} cm^{-3}) and hole (10^{16} cm^{-3}) trap states. In addition, we show that both carriers are trapped on sub-nanosecond timescales, while their depopulation occurs over tens of microseconds. Furthermore, we observe a higher mobility for holes compared to electrons, which amount to 5 and 0.01 $cm^2/(Vs)$, respectively, in agreement with the imbalance in their effective masses.[15,25] Localization of holes causes an effective loss in mobility for the holes, dropping to approximately 1.7 $cm^2/(Vs)$, while no effect can be discerned for the electrons. Knowing these kinetic parameters allows us to predict the charge carrier dynamics under AM 1.5, explaining the solar cell performance. Our newly developed DPE-TRMC methodology gives direct insight into the timescales involved with population and depopulation of the various trap states in $Cs_2AgBiBr_6$, essential for the design of more efficient devices.

RESULTS AND DISCUSSION

Perovskite synthesis and characterization

$Cs_2AgBiBr_6$ thin films of approximately 150 nm were prepared by spin-coating a 0.5-M solution of the precursor powders in DMSO onto a quartz (for TRPL and TRMC) or borosilicate (for TA) substrate, as detailed in Note S1. We confirmed the

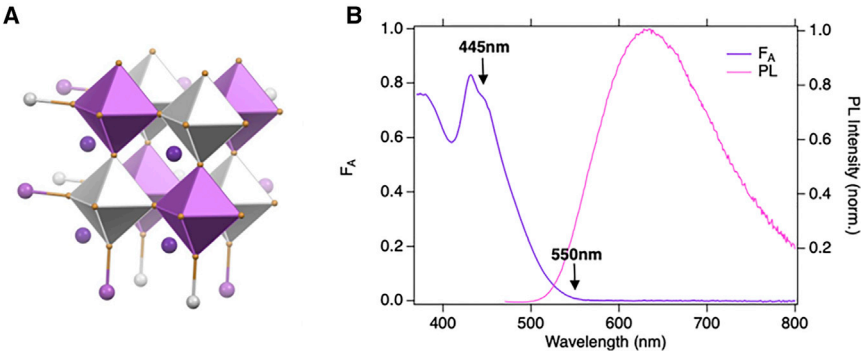

Figure 1. $Cs_2AgBiBr_6$ double-metal perovskite

(A and B) (A) General $A_2B'B''X_6$ perovskite structure, where purple and gray indicate the B′ and B″ ions and respective octahedra. In (B), the fraction of absorbed light (F_A in purple) and photoluminescence (PL in pink) spectra are shown for the $Cs_2AgBiBr_6$ analyzed in this study. The excitation wavelengths for the main DPE-TRMC experiments are indicated by the black arrows.

formation of the desired cubic phase, whose structure is schematically depicted in Figure 1A by X-ray diffraction measurements (Note S2 and Figure S1A). Scanning electron microscopy (SEM) imaging (Note S2 and Figure S1B) revealed a smooth and homogeneous coverage of the substrate, with grain sizes varying from 100 to 400 nm. From absorption measurements we found an indirect and a direct band gap at 2.57 and 3.05 eV, respectively, in line with previously reported values.[20,26] The fraction of absorbed light, F_A, and PL are shown in Figure 1B in purple (left axis) and pink (right axis), respectively. Transmission and reflection spectra as well as temperature-dependent absorption and PL are provided in Note S3 and Figures S2 and S3, respectively. The large Stokes shift observed for the PL has been associated with the radiative emission of electrons in color centers back to the valence band. Color centers are optically active anionic vacancies that are formed in $Cs_2AgBiBr_6$ under common synthesis conditions.[27,28]

DPE-TRMC

The DPE-TRMC results for 445–445 nm double excitation (above the band-gap excitation) are shown in Figure 2A. The red TRMC trace in the upper panel corresponds to the photoconductance trace, ΔG_1, generated using a single laser pulse at $t = 0$ with intensity I_1. The orange trace, labeled with ΔG_2, is induced by a single excitation at a delay time, $t_D = 500$ ns with intensity I_2. Both types of excitations were performed at 445 nm (2.79 eV). As the excitation intensities of I_1 and I_2 are very close, the recorded ΔG_1 and ΔG_2 traces present similar kinetics and magnitudes. Since the photoconductivity of a material, ΔG, is proportional to the number of charge carriers and their mobilities, the observed rapid decay of the signal indicates swift recombination and/or immobilization of charge carriers. The measured lifetimes are in line with what has been previously reported regarding the fast trapping and recombination in $Cs_2AgBiBr_6$ perovskites.[21,23,29] Figure 2A shows, in green, the DPE-TRMC signal, ΔG_{DPE} induced by excitation using two subsequent laser pulses with a delay of 500 ns. The ΔG_{DPE} signal shows how both laser pulses lead to two distinct signals. Interestingly, the second photoconductance signal in the ΔG_{DPE} trace is clearly larger than ΔG_2, although identical laser intensities are used. The difference is even more clear after subtracting ΔG_1 and ΔG_2 from ΔG_{DPE}, as shown in blue in the lower part of panel A and denoted as ΔG_{Change}. A sizable increment of the signal of approximately 10% induced by the second laser pulse is observed in the specific case of Figure 2A. This procedure has been repeated for multiple delay times, and the results (ΔG_{Change}) are plotted as a function of different delay times in Figure 2B.

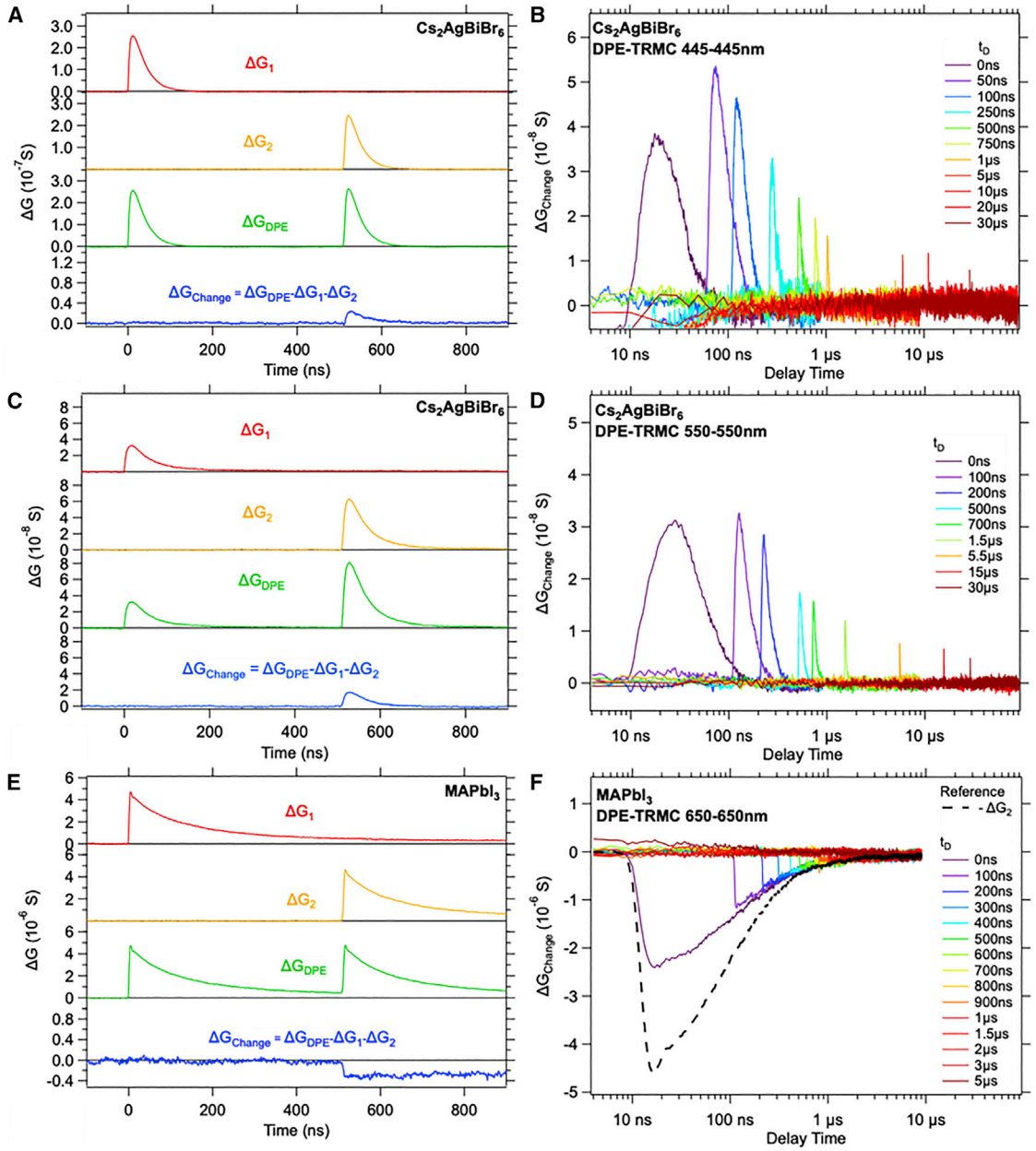

Figure 2. DPE-TRMC measurements

(A–F) (A) $Cs_2AgBiBr_6$ upon 445–445 nm double-pulsed excitation, (C) $Cs_2AgBiBr_6$ upon 550–550 nm pulsed excitation, and (E) $MAPbI_3$ upon 650–650 nm pulsed excitation. The red lines correspond to the traces obtained by the first pulse excitation only, the orange from the second, and the green a combination of the 2. The blue traces, ΔG_{Change}, are the DPE-TRMC signals corrected for both first and second excitations. (B, D, and F) Corrected DPE-TRMC signals obtained at different delay times ranging from 0 ns to 30 µs for $Cs_2AgBiBr_6$ and $MAPbI_3$. $Cs_2AgBiBr_6$ measurements have been performed using 1.4×10^{13} photons/cm^2 per pulse at 445 nm and 1.2×10^{14} photons/cm^2 at 550 nm, while a lower intensity of 2.6×10^{12} photons/cm^2 per pulse has been used for $MAPbI_3$.

From here, we can conclude that the presence of the first laser pulse leads to an enhancement of the photoconductance generated by the second pulse even up to delay times of 30 µs. Note that this enhanced photoconductance is not related to a rise in photoinduced absorption, since TA measurements display a strong bleach at 445 nm. Instead, it seems that the increase is due to non-mobile photo-physical products, that are still present 30 µs after the first laser pulse.

The above measurements are conducted in a resonant microwave cell, which has a response time of 18 ns. To further investigate the photoconductance enhancement at short delay times (t_D = 50–100 ns), we have also performed DPE-TRMC in a non-resonant TRMC cell, which has a response time of approximately 1 ns. The results, presented in Note S4 and Figure S4A, show how the positive effect of the first pulse on the photoconductance at short delay times is counteracted by a negative "bleaching" of the TRMC signal. Similar to TA measurements, a bleaching of the TRMC signal could be due to a reduced charge carrier population in the band edge states for the second excitation. Furthermore, the excess charges induced by the first pulse will lead to an enhancement of second-order recombination processes, which would lower the magnitude of the DPE-TRMC signal at short delay times.

To investigate whether the enhancement is related to a specific excitation wavelength, we also performed DPE-TRMC experiments exciting close to the band edges, at 550–550 nm (note that here, I_2 is almost two times larger than I_1). The results are shown in Figures 2C and 2D. Despite the fact that the signal heights of ΔG_1, ΔG_2, ΔG_{DPE}, and ΔG_{Change} are much smaller due to the reduced optical absorption, remarkable similarities with those obtained at 445–445 nm are found. Although we cannot completely exclude some band tail absorption by the indirect band gap, the presence of a substantial PL intensity at 550 nm wavelength suggests that excitation at this wavelength can be related to the excitation of electrons to the optically active color centers. This optical process leads to the presence of mobile holes in the valence band, obviously giving rise to similar photophysical products as for excitations at 445 nm, explaining the similar observations for our DPE-TRMC experiments.

In sharp contrast to $Cs_2AgBiBr_6$, we observed negative ΔG_{Change} signals for other perovskites, such as methylammonium lead iodide ($MAPbI_3$). A direct comparison between $Cs_2AgBiBr_6$ and $MAPbI_3$ can be made by comparing Figure 2A with **2e** for a 500-ns delay time, and **2b** with **2f** for a complete overview of the ΔG_{Change} signals as a function of varying delay times. From Figure 2F, it is evident there is a clear match of the single-pulse photoconductance decay and the decreasing trend of the maxima of the ΔG_{Change} signals. We link this behavior to the decreased charge carrier population in the band edge states and enhanced second-order recombination. This behavior can be observed for >1 μs, after which the ΔG_{Change} signal is completely reduced to zero. This means that for longer t_D values, the second excitation leads to identical results in both single and DPE modes. Similar results are obtained for the triple cation, lead halide perovskites as shown in Note S5 and Figure S5. Although the charge carrier decay times are much slower than that of $MAPbI_3$, we observe negative ΔG_{Change} signals independent of the delay time. Most important, this is not the case for $Cs_2AgBiBr_6$; even after tens of microseconds after the microwave signal of the first pulse, the ΔG_{DPE} signal induced by the second laser pulse is higher than ΔG_2 only. To highlight the unicity of these results in $Cs_2AgBiBr_6$, we performed additional measurements on a sample containing a small fraction of antimony, namely $Cs_2AgBi_{0.8}Sb_{0.2}Br_6$. The characterization and DPE-TRMC results can be found in Note S6 and Figure S6. As for $MAPbI_3$, the ΔG_{Change} of $Cs_2AgBi_{0.8}Sb_{0.2}Br_6$ is negative at all of the investigated delay times, and the maxima of the ΔG_{Change} as a function of the delay times follow the decay trend of the ΔG_2 signal without a first pulse.

Modeling

Multiple phenomena could be responsible for an enhanced photoconductance during a DPE-TRMC experiment, such as (1) an increased absorption, (2) release of

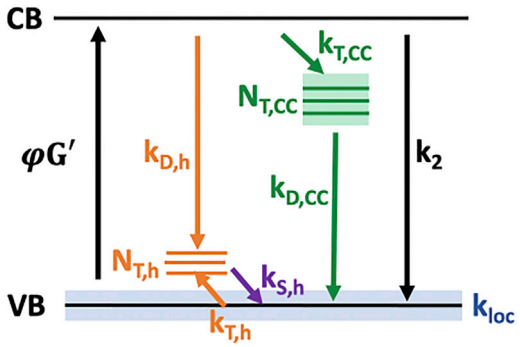

Scheme 1. Schematic representation of the main kinetic processes and rate constants included in the TRMC and DPE-TRMC modeling

$\varphi G'$ represents the charge carrier generation term. Following generation, sub-nanosecond localization occurs, the effects of which can be mainly observed on the holes. This process proceeds with a specific rate constant, k_{loc} (blue). Electrons can be trapped into deep trap states, the so-called color centers (CCs), and from there recombine with holes in the valence band (green process). Trapped holes can either recombine with free electrons (orange process) or escape from shallow trapping by thermal excitation (purple arrow). Second-order band-to-band recombination is shown in black.

trapped electrons/holes, (3) increase in the temperature of the $Cs_2AgBiBr_6$ layer, and/or (4) a higher yield of free mobile carriers due to the partial saturation of trap states by the first laser pulse. The first hypothesis (i.e., an increased absorption) is invalidated by the observation that the optical absorption is reduced (i.e., bleached) at 445 nm by TA measurements on $Cs_2AgBiBr_6$.[30] A release of trapped carriers by the second pulse could also lead to an enhancement of the photoconductance in a DPE-TRMC measurement. We disprove this hypothesis by performing DPE-TRMC measurements with a first excitation at 445 nm (above the band gap), followed by an intense 600 nm (below the band gap) pulse. Since deep traps have energy levels within the band gap of the material (i.e., broad PL is observed between 500 and 700 nm), a second 600-nm excitation should provide sufficient energy to release trapped carriers. If de-trapping would occur, the ΔG_{DPE} signal would be expected to show changes in magnitude (increase) and in decay kinetics due to the presence of a higher concentration of mobile carriers. However, we did not observe evidence of such a process, as shown in Note S4 and Figure S4B. Here, ΔG_{Change} is equal to zero at all delay times, indicating that no release of trapped carriers was induced by the second 600-nm laser pulse. As such, the DPE-TRMC trace is identical to the sum of ΔG_1 and ΔG_2 traces. Furthermore, we can exclude an increase in temperature as a possible explanation for the enhanced photoconductance as demonstrated in the supplemental note in Note S7 and Figure S7.

Having excluded options (1), (2) and (3), we postulate a higher yield of free mobile carriers, due to relatively less trapping within the response time, since the traps are still populated from the first pulse. To verify this, we modeled the DPE-TRMC traces, with a kinetic model accounting for fast localization of carriers, electron trapping into color centers, and shallow hole trapping. All of these processes, schematically represented in Scheme 1, have been separately observed in previous

Table 1. Fitting parameters for the $Cs_2AgBiBr_6$ sample analyzed in this study

k_{loc} (s^{-1})	k_2 (cm^3/s)	$N_{T,CC}$ (cm^{-3})	$k_{T,CC}$ (cm^3/s)	$k_{D,CC}$ (cm^3/s)	$N_{T,h}$ (cm^{-3})	$k_{T,h}$ (cm^3/s)	$k_{D,h}$ (cm^3/s)	$k_{S,h}$ (s^{-1})
1.0×10^{9}[a]	5.0×10^{-11}	2.0×10^{15}	5.0×10^{-8}	6.0×10^{-9}	1.2×10^{16}	6.5×10^{-7}	9.0×10^{-11}	5.0×10^{5}

[a]At the highest intensity of I_1, a 3-times higher localization rate is used.

studies.[20,21,23] We used a set of coupled differential equations (Equations 1, 2, 3, 4, and 5) to model the concentration of carriers in the different states. Namely, n_e is the time-dependent electron concentration in the conduction band, $n_{h,deloc}$ and $n_{h,loc}$ represent the hole concentrations before and after localization, and $n_{T,CC}$ and $n_{T,h}$ are the electron and hole concentrations in their corresponding trap states. Electron localization has been excluded since it led to no effective change in either mobility or decay kinetics. The charge carrier generation term, G', accounts for the intensity, I, and the temporal profile of the laser pulse. Since the exciton binding energy in $Cs_2AgBiBr_6$ is appreciable,[15] the excitation intensities were corrected for the free carrier generation yield, φ (i.e., the number of free carriers over the total number of excitations). As further discussed and detailed in the supplemental information, this yield has been derived from the fittings to the experimental data points and related to the exciton binding energy with the help of the Saha model. In the following discussion, G'_1 is used as generation term of ΔG_1, G'_2 for ΔG_2, and G'_{1+2} for ΔG_{DPE}. As shown in Scheme 1, the trapping and de-trapping rate constants are k_T and k_D, respectively, while the localization rate constant is k_{loc}. Lastly, $k_{S,h}$ is the de-trapping rate constant accounting for the release of holes back into the valence band. To facilitate the visualization, the same color scheme adopted for the processes in Scheme 1 is used in the equations:

$$\frac{dn_e}{dt} = \varphi G' - k_2 n_e(n_{h,deloc} + n_{h,loc}) - k_{T,CC}(N_{T,CC} - n_{T,CC})n_e - k_{D,h}n_{T,h}n_e \quad \text{(Equation 1)}$$

$$\frac{dn_{h,deloc}}{dt} = \varphi G' - k_{loc}n_{h,deloc} - k_2 n_e(n_{h,deloc} + n_{h,loc}) - k_{T,h}(N_{T,h} - n_{T,h})n_{h,deloc} \quad \text{(Equation 2)}$$

$$\frac{dn_{h,loc}}{dt} = k_{loc}n_{h,deloc} - k_2 n_e(n_{h,deloc} + n_{h,loc}) - k_{D,CC}n_{T,CC}n_{h,loc} + k_{S,h}n_{T,h} \quad \text{(Equation 3)}$$

$$\frac{dn_{T,CC}}{dt} = k_{T,CC}(N_{T,CC} - n_{T,CC})n_e - k_{D,CC}n_{T,CC}n_{h,loc} \quad \text{(Equation 4)}$$

$$\frac{dn_{T,h}}{dt} = k_{T,h}(N_{T,h} - n_{T,h})n_{h,deloc} - k_{D,h}n_{T,h}n_e - k_{S,h}n_{T,h} \quad \text{(Equation 5)}$$

For the fitting of the DPE-TRMC signals, we multiplied the calculated concentration curves with their mobility values, μ, according to

$$\Delta G = e\beta L\left(n_e\mu_e + n_{h,deloc}\mu_{h,deloc} + n_{h,loc}\mu_{h,loc}\right) \quad \text{(Equation 6)}$$

where e is the elementary charge, β is a waveguide geometrical factor, and L is the sample thickness. On the basis of the different electron and hole effective masses in $Cs_2AgBiBr_6$, a major hole contribution to the ΔG signal magnitude is expected.[15] A hole mobility of 5 $cm^2/(Vs)$ was estimated from the model for the non-localized holes, quickly reducing to 1.7 $cm^2/(Vs)$, in agreement with the sub-nanosecond process reported by Wright et al.,[21] while the electron mobility is very low, approximately 0.01 $cm^2/(Vs)$. Despite the negligible contribution of the electrons to the photoconductance signal (as per Equation 6), their concentration has a strong impact on the observed decay kinetics.

The profiles G'_1, G'_2 and G'_{1+2} for G' in Equations 1 and 2 have been constructed on the basis of the temporal profile and intensities, I_1 and I_2, of both laser pulses. The corresponding yields φ of free carrier generation are calculated taking into account the intensity of each laser pulse. Moreover, in case of G'_{1+2}, φ_2 has been determined

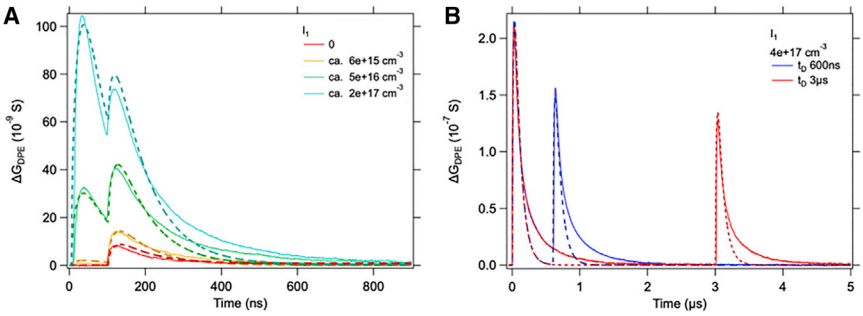

Figure 3. Experimental DPE-TRMC traces (solid lines) and corresponding fits (dashed lines) of $Cs_2AgBiBr_6$

(A and B) In (A), DPE-TRMC traces at variable I_1 and constant I_2 with a fixed of t_D=100 ns are shown. In (B), traces are given for fixed laser intensities, but at t_D = 600 ns and at t_D = 3 µs at I_2 of 2 × 10^{16} cm $^{-3}$.

accounting for the number of free carriers present at t_D after the first excitation. The kinetic parameters have been determined by iteratively fitting the ΔG_{DPE} traces recorded for a large variety of experiments with different intensities and delay times. Ultimately, the model is able to fit the DPE-TRMC traces accurately using the corresponding G'_{1+2} generation profile, as shown in Figure 3. The fitting parameters are reported in Table 1. In Figure 3A, t_D has been set to 100 ns, at which delay we recorded the maximum enhancement in photoconductance (see Figure 2B). Here, the intensity of the first pulse, I_1, has been varied from 0 to 10^{17} charges/cm^3, while the intensity of the second pulse, I_2, is kept constant. As is clear from Figure 3A, the higher I_1, the larger the absolute rise in photoconductance upon the second pulse. Furthermore, the magnitude of the enhancement decreases over time, as shown in Figure 3B for t_D = 600 ns and t_D = 3 µs. Also, this aspect is included in our model as clearly shown by the overlap between DPE-TRMC traces and our fits. For completeness, we also show the TRMC traces using only a single laser pulse and corresponding fits using the same model, showing decent overlap in Note S8 and Figure S8. Thus, variation in delay time as well as variation in intensity as presented in Figure 3 confirm the validity of our kinetic model, which clearly captures the main kinetic processes in $Cs_2AgBiBr_6$. From the time-dependent concentrations of the carriers in the different states (as described by Equations 1, 2, 3, 4, and 5), and reported in Note S8 and Figure S9), we can draw some important conclusions. First, as expected, the delocalized holes do not play a relevant role in the observed photoconductance, as they disappear within the response time of our measurements. Nonetheless, their presence in the modeling is necessary, as hole trapping competes with the localization process. Second, in contrast to the fast localization and trapping, the de-trapping of both electrons and holes extends into the microsecond regime. As shown in Note S8 and Figure S9B, both carriers remain trapped for several microseconds after excitation. In conclusion, the slow de-trapping of localized carriers in $Cs_2AgBiBr_6$ is the reason that, in a double-pulse experiment, the second pulse yields a larger signal than in the absence of the first pulse. The fact that the DPE-TRMC measurements on $MAPbI_3$ show an opposite sign for ΔG_{Change}, independent of the delay time, implies that population of trap states induced by the first pulse is not prevailing.

In previous TRMC studies we have reported the presence of relatively high concentrations of trap states (10^{16}–10^{17} cm^{-3}) for both electrons and holes.[23,29] With our new model and iterative analysis of the DPE-TRMC traces at different intensities and delay times, we are now able to quantify these concentrations more accurately

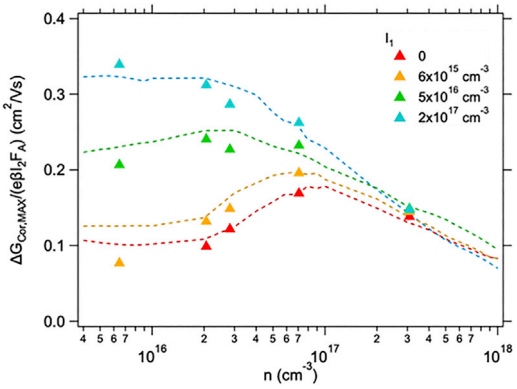

Figure 4. Intensity-dependent DPE-TRMC enhancement

Plot of the I_2 normalized maximum ΔG_{Cor} values versus excitation density, n induced by I_2. The vertical axis is a measure of the $\varphi\Sigma\mu$ product. The intensity of the first pulse increases from red ($I_1 = 0$) to blue ($I_1 = 4 \times 10^{11}$ photons/cm^2 pulse). The delay time was kept constant at $t_D = 100$ ns. The dashed lines have been simulated for different I_1 over a broader range of I_2. We note that the lowest I_1 and I_2 experimental points (i.e., red and orange), at $n = 6 \times 10^{15}$ cm^{-3}, are affected by poor signal-to-noise ratio. For this reason, the specific point at $I_1 = 0$ is not shown in the graph.

and, more important, obtain insights regarding the depopulation times. To quantify the trap densities in more detail, we performed DPE-TRMC measurements with various intensities of the first and second pulse but keeping t_D constant at 100 ns. To study the changes induced by the first pulse on the second excitation, we subtracted ΔG_1, from the ΔG_{DPE} signal.

$$\Delta G_{Cor} = \Delta G_{DPE} - \Delta G_1 \quad \text{(Equation 7)}$$

Next, the maximum values of ΔG_{Cor} were normalized for the incident intensity of the second laser pulse, I_2, yielding the product of the free carrier generation yield, φ, and the sum of electron and hole mobilities, $\Sigma\mu$, according to

$$\varphi \sum \mu = \frac{\Delta G_{Cor,MAX}}{e\beta I_2 F_A}, \quad \text{(Equation 8)}$$

and these values are plotted in Figure 4. From Figure 4, we can observe that with $I_1 = 0$, the intensity normalized photoconductance maxima initially increase with higher I_2, showing a maximum at $I_2 = 7 \times 10^{16}$ cm^{-3}, followed by a decrease. We have previously observed such behavior, and this was explained by a dominant trap filling process at low photon fluences, while at higher intensities, higher order recombination prevails.[29] Adding to this, it must be noted that the yield of free carrier generation, φ, is strongly intensity dependent. As shown in Note S9 and Figure S10B, for exciton bindings energies in the range of 100–200 meV, φ can decrease more than a factor of 4 in the intensity range analyzed.

By stepwise increasing I_1 up to 2×10^{17} cm^{-3} and keeping $t_D = 100$ ns, the trap filling process gradually disappears. The $\varphi\Sigma\mu$ values obtained for maximum I_1 follow the more commonly observed intensity-dependent behavior we reported for several lead-containing perovskite thin films, (i.e., lower values with higher intensities due to enhanced higher order recombination during the response time of our measurements).[31] Since holes are the major contributors to the observed photoconductance signals, we conclude that the first laser pulse leads to the rapid population of hole traps. The higher the occupation level of these states, the higher the increase in the second laser pulse. The highest product of $\varphi\Sigma\mu$ is approximately 0.35 cm^2/(Vs) (as visible from the blue points in Figure 4). Since the hole mobility was found to amount to 1.7 cm^2/(Vs), this

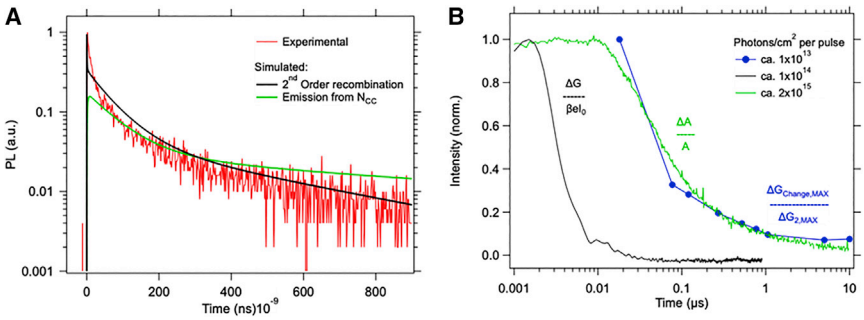

Figure 5. Comparison with TRPL and TA

(A) Comparison of the experimental (red) and simulated (black and green) TRPL signals. The simulation has been done using the same kinetic parameters derived from DPE-TRMC measurements at an excitation intensity of approximately 4×10^{16} cm^{-3}.

(B) Normalized DPE-TRMC $\Delta G_{Change,MAX}/\Delta G_{2,MAX}$ (blue), transient absorption (green), and open cell TRMC (black) traces. The DPE-TRMC results have been normalized, accounting for the bleaching effect at $t_D = 0$ ns.

translates into a free carrier generation yield of approximately 24% at room temperature at the lowest intensity of I_2. As shown in Note S9 and Figure S10A, this implies an exciton binding energy of approximately 120–130 meV, in the range of previously reported values.[15,32,33] However, it is important to highlight that during the fitting procedure, both the mobility and φ values have been treated as variables. The found values were obtained only after iterative fittings with different laser intensities and delay times, as described in the above discussion.

Verification with time-resolved PL and TA

To corroborate our observations and kinetic model, additional TRPL measurements were performed using a TRPL system using an excitation wavelength of 405 nm (red trace in Figure 5A). In agreement with previous studies, a fast initial decay with a long-lived tail is observed.[22] We simulated the TRPL signal, applying our kinetic model with the rate constants mentioned in Table 1 and using a G' profile that represents the laser pulse with 80 ps full width at half-maximum (FWHM) and intensity used for the TRPL measurements. The simulations have been performed accounting for second-order band-to-band recombination and emission from color centers. The normalized results are shown in Figure 5A. As can be seen, the simulation reveals the presence of a fast initial decay that originates from the recombination of free electrons with delocalized holes (black). However, based on the similarities in decay kinetics on longer timescales and relative magnitudes of the simulated intensities (see Note S10 and Figure S11), both second-order recombination and trap-assisted recombination are expected to contribute to the observed long-living TRPL signals.

Moreover, we performed TA measurements and compared the decay kinetics of the TA signal with the DPE-TRMC results. In previous work, we performed a complementary TA/TRMC analysis that revealed the pathways leading to mobility losses in $Cs_2AgBiBr_6$.[30] In the present study, we focus on the charge carrier dynamics and lifetimes revealed by the two techniques. Following a similar procedure as in the analysis of TA absorption data, we normalized the maxima of ΔG_{Change} by the photoconductance maxima of ΔG_2. The normalized DPE-TRMC trend at different delay times (blue dots, cavity), the single-pulse TRMC trace (black line, open cell) and TA data (green line) are shown in Figure 5B. Furthermore, we accounted for the "bleaching" effect on the DPE-TRMC signal at $t_D = 0$ ns. Most interestingly, the lifetime of the TA

Table 2. Simulation results of the percentage contributions of the localization, second-order recombination, and trapping processes under continuous illumination. The saturation percentages of the electrons, $N_{T,CC}$, and holes, $N_{T,h}$, trap states are also reported.

	0.01 suns	0.1 suns	0.5 suns	1 sun	10 suns
Second order, %	0.001	0.001	0.002	0.002	0.003
e^- trapping, %	>99.99	>99.99	>99.99	>99.99	>99.99
$N_{T,CC}$ saturation, %	0.80	1.93	2.68	3.32	6.73
h^+ localization, %	27.78	27.79	27.81	27.86	27.90
h^+ trapping, %	72.22	72.21	72.19	72.14	72.10
$N_{T,h}$ saturation, %	0.02	0.08	0.14	0.20	0.61

signal matches the data of the DPE-TRMC results very well. Hence, we conclude that the long-lived trapped charges are responsible for the observed TA and DPE-TRMC signals. Since the mobile carriers are rapidly lost, the microsecond lifetimes can only originate by the slow release of holes from trap states close to the valence band (purple process in Scheme 1 proceeding with a rate constant of 1×10^5 s^{-1}). Accounting for the thermodynamic stability of the different defect states in $Cs_2AgBiBr_6$ reported in theoretical studies,[27,28] we speculate that the observed behavior can be caused by either silver vacancies (V_{Ag}) and/or silver-bismuth anti-sites (Ag_{Bi}). The fact that the same trend is not observed on partial substitution of Bi with Sb can be related to a change in electronic structure and defect stability induced by the substitution.

Extrapolation to solar light

Lastly, by substituting G' in Equations 1 and 2 with a continuous illumination profile corresponding to AM 1.5, we can extrapolate the charge carrier concentrations on solar illumination.[34] For the calculations, the spectral photon flux has been corrected for the fraction of absorbed light for the $Cs_2AgBiBr_6$ thin film (details can be found in Note S11 and Figure S12). The time-dependent charge carrier concentrations on continuous illumination are reported in Note S11 and Figure S13. A detailed analysis of the processes over a broad range of intensities (i.e., 0.01–10 suns) reveals that upon continuous illumination, almost all of the electrons (>99.9%) decay via trap-assisted recombination. This results in extremely low free electron densities once the equilibrium is reached (see Note S11 and Figure S13). The evident dominance of trap-assisted electron recombination over the second order process during continuous illumination further supports the hypothesis that color center emission is responsible for the steady-state PL spectral features. For the positive charge carriers, the localization process is in competition with shallow trapping, yielding to a relatively low percentage of localized but mobile holes (approximately 28%), while the majority is rapidly trapped (approximately 72%). The relative contribution percentages are summarized in Table 2 at different illumination conditions. This analysis also reveals that under AM 1.5 or even 10 suns, both electron and hole trap states in $Cs_2AgBiBr_6$ do not saturate at all, despite the fact that charges remain trapped for long periods. The immobilization and loss of carriers via trap-assisted recombination is strongly detrimental for the performance of photovoltaic devices. However, long-lived charges in surface states may be beneficial for other applications such as photocatalysis or lasing.

To conclude, in this study we have performed extensive time-resolved measurements to reveal the complex charge carrier dynamics in $Cs_2AgBiBr_6$ thin films. We developed a new method, DPE-TRMC. By exciting the sample with two laser pulses, we obtain unprecedented detailed information regarding charge trapping and the

corresponding depopulation process in $Cs_2AgBiBr_6$. Although single-pulse TRMC experiments show that all mobile charges decay within 50 ns, we found that the second pulse led to an enhanced photoconductance up to 30 μs after the first pulse. Interestingly, this effect is only present when the energy of the second pulse exceeds the band gap, meaning that this enhanced photoconductance is not related to trap release. Instead, we attribute the relatively higher photoconductivity from the second pulse to a higher yield of free charges, occurring as long as traps are populated from the first pulse. By using an intense first pulse, complete saturation of the trap states can be accomplished, yielding maximal enhancement. For $MAPbI_3$, the opposite behavior is observed, demonstrating that population of trap states by the first pulse is not prevailing, and other factors such as second-order recombination dominates. By varying wavelengths, intensities, and delay times, we obtain a full picture of the (de-)population kinetics of defects in $Cs_2AgBiBr_6$. On analysis of all of the data, a kinetic model is proposed to effectively capture the complex dynamics of photoexcited charges in the films. From the corresponding signal height, we derived a yield of 0.24, which concurs with an exciton binding energy of 120–130 meV. We found that electrons are rapidly trapped in color centers. Radiative emission of electrons from these color centers contributes to long-lived emission in agreement with the TRPL results. In line with TA observations, we conclude that holes are predominantly trapped in shallow states from which they release over many microseconds. The trap-assisted recombination, effectively depleting the concentration of electrons in the conduction band, combined with the low hole mobility (1.7 $cm^2/(Vs)$) and shallow trapping, is expected to be a major drawback of $Cs_2AgBiBr_6$ in photovoltaic devices. Despite these limitations, the long-lived charge carriers in $Cs_2AgBiBr_6$ as observed in this work can offer a suitable, lead-free alternative for other applications, such as X-ray detectors or photocatalysis.

EXPERIMENTAL PROCEDURES

Resource availability

Lead contact

Dr.Ir. Tom J. Savnije: t.j.savenije@tudelft.nl.

Materials availability

The actual measured samples have partially degraded; however, detailed protocols for sample preparation are available.

Data and code availability

The most relevant data have been reported in the document and in the supplemental information. Additional data (different intensities and excitation wavelengths) and raw file are available on request.

Characterization

In this study, we performed DPE-TRMC measurements to investigate charge carrier dynamics in $Cs_2AgBiBr_6$ thin films. This technique, analogous to the TRMC that we previously applied in several studies, some of which on $Cs_2AgBiBr_6$,[23,29] relies on the interaction of the photoexcited carriers with microwaves. As a result of photoexcitation, free charge carriers will be generated inside the material. The interaction of such free carriers with microwaves leads to a reduction in the microwave power. The normalized power charge can be converted into a photoconductance signal given as:[31]

$$\frac{\Delta P(t)}{P} = -K\Delta G(t) \qquad \text{(Equation 9)}$$

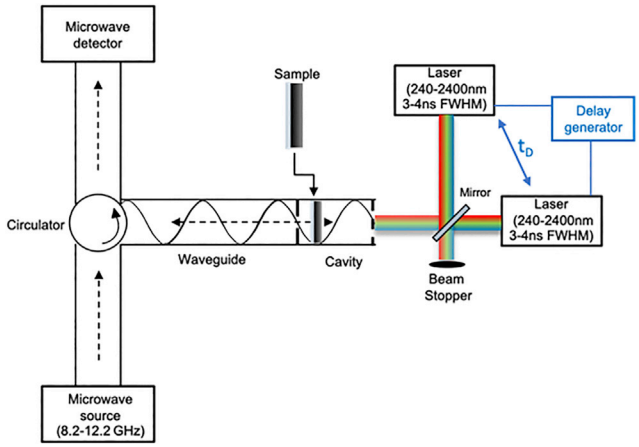

Scheme 2. Schematic representation of microwave conductance setup for single-pulse TRMC (only 1 laser active), and DPE-TRMC (with 2 lasers)

The lasers are simultaneously exciting the samples from the same direction with the help of a semitransparent mirror.

In Equation 9, P represents the microwave power, K is a predetermined sensitivity factor, and ΔG is the change in photoconductance. While ordinary TRMC is carried out with a single laser pulse, DPE-TRMC makes use of two laser pulses, delayed by means of a digital delay generator. The temporal (3.5 ns FWHM) and spatial shape of both laser pulses are very similar. A schematic representation of the setup is shown in Scheme 2. The delay times, t_D, can be varied from 0 ns to >30 μs. DPE-TRMC provides unique insight into how photoexcited species generated by the first pulse affect the yield and dynamics of carriers induced by the second pulse.

Complementarily, TA measurements were performed using an EOS multichannel pump probe TA spectrometer (Ultrafast Systems LLC). The third harmonic (355 nm) of a Nd:YAG laser (1,064 nm, 650 ps FWHM pulse duration, 1 kHZ) was used as the excitation source. Laser pulses with an energy of 4.5 μJ were focused to a spot size of 3×10^{-4} cm^{-2}, corresponding to a fluence of 2.7×10^{16} photons cm^{-2} per pulse. The probe pulse was generated using a LEUKOS super-continuum light source (200–2,400 nm, 200 mW, <1 ns) operating at 2 kHz. The white light is split into a probe and a reference beam, which is used to correct for fluctuations in the probe intensity. The reference and probe beam transmission spectra are both detected using a fiberoptics coupled multichannel spectrometer with a complementary metal oxide semiconductor (CMOS) sensor (spectral resolution of 1.5 nm).

Time-resolved PL has been performed with an Edinburgh Instrument LifeSpec-ps spectrometer. The sample was excited at 404 nm by a Hamamatsu C8898 picosecond pulsed laser diode (repetition frequency 200 kHz, intensity 6×10^{11} photons/cm^2).

SUPPLEMENTAL INFORMATION

Supplemental information can be found online at https://doi.org/10.1016/j.xcrp.2022.101055.

ACKNOWLEDGMENTS

V.M.C. and T.J.S. acknowledge funding from the Dutch Research Council (NWO), grant no. 739.017.004. H.J.J. and E.M.H. acknowledge funding from the Dutch

Research Council (NWO) under grant no. VI.Veni.192.034. H.J.J. and E.M.H. are supported further by the Advanced Research Center Chemical Building Blocks Consortium (ARC CBBC).

AUTHOR CONTRIBUTIONS

V.M.C. prepared the samples following the procedure developed in collaboration with S.A.P. Sample characterization (absorption, PL, X-ray diffraction [XRD], SEM, DPE-TRMC, and TRPL) and data analysis have been performed by V.M.C. under the supervision of T.J.S. TA measurements have been performed by H.J.J., supervised by E.M.H. The manuscript has been written by V.M.C. and T.J.S., with the contributions of E.M.H. and H.J.J.

DECLARATION OF INTERESTS

The authors declare no competing interests.

Received: June 1, 2022
Revised: July 27, 2022
Accepted: August 24, 2022
Published: September 13, 2022

REFERENCES

1. Jeong, J., Kim, M., Seo, J., Lu, H., Ahlawat, P., Mishra, A., Yang, Y., Hope, M.A., Eickemeyer, F.T., Kim, M., et al. (2021). Pseudo-halide anion engineering for α-FAPbI3 perovskite solar cells. Nature *592*, 381–385.

2. Pazoki, M., Jacobsson, T.J., Hagfeldt, A., Boschloo, G., and Edvinsson, T. (2016). Effect of metal cation replacement on the electronic structure of metalorganic halide perovskites: replacement of lead with alkaline-earth metals. Phys. Rev. B *93*, 144105–144110.

3. Lau, C.F.J., Deng, X., Zheng, J., Kim, J., Zhang, Z., Zhang, M., Bing, J., Wilkinson, B., Hu, L., Patterson, R., et al. (2018). Enhanced performance: via partial lead replacement with calcium for a CsPbI3 perovskite solar cell exceeding 13% power conversion efficiency. J. Mater. Chem. *6*, 5580–5586.

4. Wang, N., Zhou, Y., Ju, M.G., Garces, H.F., Ding, T., Pang, S., Zeng, X.C., Padture, N.P., and Sun, X.W. (2016). Heterojunction-depleted lead-free perovskite solar cells with coarse-grained B-γ-CsSnI3 thin films. Adv. Energy Mater. *6*, 1601130–1601210.

5. Shao, S., Liu, J., Portale, G., Fang, H.H., Blake, G.R., ten Brink, G.H., Koster, L.J.A., and Loi, M.A. (2018). Highly reproducible Sn-based hybrid perovskite solar cells with 9% efficiency. Adv. Energy Mater. *8*, 1702019.

6. Kopacic, I., Friesenbichler, B., Hoefler, S.F., Kunert, B., Plank, H., Rath, T., and Trimmel, G. (2018). Enhanced performance of germanium halide perovskite solar cells through compositional engineering. ACS Appl. Energy Mater. *1*, 343–347.

7. Chen, M., Ju, M.G., Garces, H.F., Carl, A.D., Ono, L.K., Hawash, Z., Zhang, Y., Shen, T., Qi, Y., Grimm, R.L., et al. (2019). Highly stable and efficient all-inorganic lead-free perovskite solar cells with native-oxide passivation. Nat. Commun. *10*, 16–18.

8. Cao, J., and Yan, F. (2021). Recent progress in tin-based perovskite solar cells. Energy Environ. Sci. *14*, 1286–1325.

9. Liu, X., Wang, Y., Wu, T., He, X., Meng, X., Barbaud, J., Chen, H., Segawa, H., Yang, X., and Han, L. (2020). Efficient and stable tin perovskite solar cells enabled by amorphous-polycrystalline structure. Nat. Commun. *11*, 2678–2687.

10. Zhang, Z., Liang, Y., Huang, H., Liu, X., Li, Q., Chen, L., and Xu, D. (2019). Stable and highly efficient photocatalysis with lead-free double-perovskite of Cs2AgBiBr6. Angew. Chem. Int. Ed. Engl. *58*, 7263–7267.

11. Chen, P., Huang, Y., Shi, Z., Chen, X., and Li, N. (2021). Improving the catalytic CO2 reduction on Cs2AgBiBr6 by halide defect engineering: a DFT study. Materials *14*, 2469.

12. Pan, W., Wu, H., Luo, J., Deng, Z., Ge, C., Chen, C., Jiang, X., Yin, W.J., Niu, G., Zhu, L., et al. (2017). Cs2AgBiBr6 single-crystal X-ray detectors with a low detection limit. Nat. Photonics *11*, 726–732.

13. Wu, C., Zhang, Q., Liu, Y., Luo, W., Guo, X., Huang, Z., Ting, H., Sun, W., Zhong, X., Wei, S., et al. (2018). The dawn of lead-free perovskite solar cell: highly stable double perovskite Cs2AgBiBr6 film. Adv. Sci. *5*, 2–9.

14. Savory, C.N., Walsh, A., and Scanlon, D.O. (2016). Can Pb-free halide double perovskites support high-efficiency solar cells? ACS Energy Lett. *1*, 949–955.

15. Biega, R.I., Filip, M.R., Leppert, L., and Neaton, J.B. (2021). Chemically localized resonant excitons in silver-pnictogen halide double perovskites. J. Phys. Chem. Lett. *12*, 2057–2063.

16. Hoye, R.L.Z., Eyre, L., Wei, F., Brivio, F., Sadhanala, A., Sun, S., Li, W., Zhang, K.H.L., MacManus-Driscoll, J.L., Bristowe, P.D., et al. (2018). Fundamental carrier lifetime exceeding 1 Ms in Cs2AgBiBr6 double perovskite. Adv. Mater. Interfac. *5*, 1800464–1800469.

17. Bibi, A., Lee, I., Nah, Y., Allam, O., Kim, H., Quan, L.N., Tang, J., Walsh, A., Jang, S.S., Sargent, E.H., and Kim, D.H. (2021). Lead-free halide double perovskites: toward stable and sustainable optoelectronic devices. Mater. Today *49*, 123–144.

18. Fan, P., Peng, H.X., Zheng, Z.H., Chen, Z.H., Tan, S.J., Chen, X.Y., Luo, Y.D., Su, Z.H., Luo, J.T., and Liang, G.X. (2019). Single-source vapor-deposited Cs2AgBiBr6 thin films for lead-free perovskite solar cells. Nanomaterials *9*, 1760.

19. Longo, G., Mahesh, S., Buizza, L.R.V., Wright, A.D., Ramadan, A.J., Abdi-Jalebi, M., Nayak, P.K., Herz, L.M., and Snaith, H.J. (2020). Understanding the performance-limiting factors of Cs2AgBiBr6double-perovskite solar cells. ACS Energy Lett. *5*, 2200–2207.

20. Zelewski, S.J., Urban, J.M., Surrente, A., Maude, D.K., Kuc, A., Schade, L., Johnson, R.D., Dollmann, M., Nayak, P.K., Snaith, H.J., et al. (2019). Revealing the nature of photoluminescence emission in the metal-halide double perovskite Cs2AgBiBr6. J. Mater. Chem. C *7*, 8350–8356.

21. Wright, A.D., Buizza, L.R.V., Savill, K.J., Longo, G., Snaith, H.J., Johnston, M.B., and Herz, L.M. (2021). Ultrafast excited-state localization in Cs2AgBiBr6Double perovskite. J. Phys. Chem. Lett. *12*, 3352–3360.

22. Slavney, A.H., Hu, T., Lindenberg, A.M., and Karunadasa, H.I. (2016). A bismuth-halide double perovskite with long carrier recombination lifetime for photovoltaic

applications. J. Am. Chem. Soc. *138*, 2138–2141.

23. Bartesaghi, D., Slavney, A.H., Gélvez-Rueda, M.C., Connor, B.A., Grozema, F.C., Karunadasa, H.I., and Savenije, T.J. (2018). Charge carrier dynamics in Cs2AgBiBr6 double perovskite. J. Phys. Chem. C Nanomater. Interfaces *122*, 4809–4816.

24. Pollock, T.P., and Schlenker, C.W. (2021). Charge trapping dynamics revealed in CH3NH3PbI3by ultrafast multipulse spectroscopy. J. Phys. Chem. C *125*, 18834–18840.

25. Zhang, H., Debroye, E., Zheng, W., Fu, S., Virgilio, L.D., Kumar, P., Bonn, M., and Wang, H.I. (2021). Highly mobile hot holes in Cs2AgBiBr6 double perovskite. Sci. Adv. *7*, eabj9066.

26. Schade, L., Wright, A.D., Johnson, R.D., Dollmann, M., Wenger, B., Nayak, P.K., Prabhakaran, D., Herz, L.M., Nicholas, R., Snaith, H.J., and Radaelli, P.G. (2019). Structural and optical properties of Cs 2 AgBiBr 6 double perovskite. ACS Energy Lett. *4*, 299–305.

27. Xiao, Z., Meng, W., Wang, J., and Yan, Y. (2016). Thermodynamic stability and defect chemistry of bismuth-based lead-free double perovskites. ChemSusChem *9*, 2628–2633.

28. Li, T., Zhao, X., Yang, D., Du, M.H., and Zhang, L. (2018). Intrinsic defect properties in halide double perovskites for optoelectronic applications. Phys. Rev. Appl. *10*, 041001.

29. Hutter, E.M., Gélvez-Rueda, M.C., Bartesaghi, D., Grozema, F.C., and Savenije, T.J. (2018). Band-like charge transport in Cs2AgBiBr6and mixed antimony-bismuth Cs2AgBi1-XSbxBr6Halide double perovskites. ACS Omega *3*, 11655–11662.

30. Jöbsis, H.J., Caselli, V.M., Askes, S.H.C., Garnett, E.C., Savenije, T.J., Rabouw, F.T., and Hutter, E.M. (2021). Recombination and localization: unfolding the pathways behind conductivity losses in Cs2AgBiBr6 thin films. Appl. Phys. Lett. *119*, 131908.

31. Savenije, T.J., Guo, D., Caselli, V.M., and Hutter, E.M. (2020). Quantifying charge-carrier mobilities and recombination rates in metal halide perovskites from time-resolved microwave photoconductivity measurements. Adv. Energy Mater. *10*, 1903788–1903812.

32. Steele, J.A., Pan, W., Martin, C., Keshavarz, M., Debroye, E., Yuan, H., Banerjee, S., Fron, E., Jonckheere, D., Kim, C.W., et al. (2018). Photophysical pathways in highly sensitive Cs2AgBiBr6 double-perovskite single-crystal X-ray detectors. Adv. Mater. *30*. e1804450–7.

33. Kentsch, R., Scholz, M., Horn, J., Schlettwein, D., Oum, K., and Lenzer, T. (2018). Exciton dynamics and electron-phonon coupling affect the photovoltaic performance of the Cs2AgBiBr6 double perovskite. J. Phys. Chem. C *122*, 25940–25947.

34. Guo, D., Caselli, V.M., Hutter, E.M., and Savenije, T.J. (2019). Comparing the calculated fermi level splitting with the open-circuit voltage in various perovskite cells. ACSEnergy Lett. *4*, 855–860.